Nanoscale Horizons

COMMUNICATION

Check for updates

Enhanced stability and sustained delivery of structurally dense DNA nanostructures *via* a biodegradable hydrogel platform

Youngjin Choi,†[a] Yeonju Song,†[bc] Bo Kyung Cho,[a] Sang Jin Baek,[ad] Jin Myeong Wang,[a] Su Hyun Seok,[efg] William M. Shih,[efg] Junsang Doh, [iD] *[chi] Youngmee Jung [iD] *[bj] and Ju Hee Ryu*[ad]

DNA nanostructures offer programmable architectures with precise ligand arrangement, yet their *in vivo* utility is often limited by structural fragility and rapid systemic clearance. Here, we present a robust platform for the sustained delivery of structurally dense, multi-helical square block DNA nanostructures (SQBs) by encapsulating them within a biodegradable hydrogel composed of thiolated hyaluronic acid (HA) and gelatin. Distinct from DNA-based hydrogels where the DNA network serves as the structural matrix, this platform employs a decoupled architecture that entraps SQBs as discrete nanoparticles within a tunable polymeric matrix. This platform is engineered to maintain an Mg^{2+}-rich microenvironment to preserve the structural integrity of SQB cargo, as evidenced by the intact morphology of nanostructures recovered from the matrix, while allowing independent control over degradation and release kinetics. *In vitro*, encapsulated SQBs retained their electrophoretic stability and exhibited release profiles governed by the hydrogel's crosslinking density and gelatin content. Importantly, SQB-hydrogel hybrids demonstrated sustained intracellular uptake in RAW 264.7 macrophages for up to 5 days, whereas free SQBs were rapidly internalized and cleared within 3 days. *In vivo* subcutaneous administration further confirmed that the hybrid system maintained detectable fluorescence for 10 days, significantly outperforming free SQBs, which were cleared within 24 hours. These findings establish a versatile hydrogel framework that effectively serves as a sustained depot for complex DNA nanostructures, offering a generalizable strategy for their localized and long-term deployment in therapeutic applications.

New concepts

This work introduces a versatile platform for the sustained delivery of structurally dense, multi-helical DNA nanostructures by integrating them into a biodegradable hydrogel matrix. While most hydrogel-based nucleic acid systems target short oligonucleotides or simple tetrahedral motifs, this study supports larger and complex DNA origami structures that are otherwise prone to rapid clearance and degradation. The dual-crosslinked hyaluronic acid/gelatin hydrogel creates a physiologically compatible, Mg^{2+}-rich microenvironment that preserves the nanostructure without requiring covalent modification. By modulating the ratios of hyaluronic acid, gelatin, and maleimide, the degradation of the hydrogel and the corresponding release of intact square block DNA nanostructures (SQBs) can be tuned. Notably, this system employs a decoupled architecture where the hydrogel matrix and the DNA nanoparticle function independently, allowing for scalable optimization of release kinetics without altering the nanostructure design. By overcoming structural fragility and unfavorable pharmacokinetics, this approach broadens the applicability of DNA nanotechnology in therapeutic contexts requiring multivalent interactions, spatial ligand control, or prolonged bioactivity, providing a generalizable design framework for future translational applications.

1. Introduction

DNA nanostructures have emerged as powerful tools for biomedical applications due to their highly programmable architecture, nanoscale precision, and the ability to spatially

[a] *Medicinal Materials Research Center, Biomedical Research Institute, Korea Institute of Science and Technology (KIST), Seoul, Republic of Korea. E-mail: jhryu@kist.re.kr*

[b] *Biomaterials Research Center, Biomedical Research Institute KIST, Seoul, Republic of Korea. E-mail: winnie97@kist.re.kr*

[c] *Department of Materials Science and Engineering, Seoul National University, 1 Gwanak-ro, Gwanak-gu, Seoul, Republic of Korea. E-mail: jsdoh@snu.ac.kr*

[d] *KU-KIST Graduate School of Converging Science and Technology, Korea University, Seoul, Republic of Korea*

[e] *Department of Cancer Biology, Dana-Farber Cancer Institute, Harvard Medical School, Boston, MA, USA*

[f] *Wyss Institute for Biologically Inspired Engineering at Harvard University, Boston, MA, USA*

[g] *Department of Biological Chemistry and Molecular Pharmacology, Harvard Medical School, Boston, MA, USA*

[h] *Research Institute of Advanced Materials, Seoul National University, Seoul, Korea*

[i] *Institute of Engineering Research: SOFT Foundry Institute, Bio-MAX Institute, Seoul National University, Seoul, 08826, Republic of Korea*

[j] *School of Electrical and Electronic Engineering, YU-KIST Institute, Yonsei University, Seoul, Republic of Korea*

† These authors contributed equally to this work.

organize bioactive ligands in defined patterns.[1,2] These ligand arrangements are determined by the geometric configuration of the DNA scaffold, which is constructed from rigid DNA helices precisely assembled at specific distances and angles.[3,4] Such spatial control enables DNA nanostructures to trigger predictable biological responses through optimized ligand–receptor interactions, as demonstrated in previous studies employing DNA origami platforms to regulate caspase-9 activation, B-cell and T-cell signaling, insulin receptor clustering, cancer therapies, and thrombolytic activity.[5–12] However, the biological efficacy of these platforms is strictly contingent upon maintaining their precise three-dimensional conformation against physiological challenges.

Despite these capabilities, the therapeutic performance of DNA nanostructures *in vivo* remains limited. Their structural fragility under physiological conditions leads to nuclease-mediated degradation, while rapid systemic clearance restricts their local retention and diminishes biological efficacy.[13–19] Although protective strategies—including lipid encapsulation, protein shielding, cationic polymer coatings, and covalent stabilization—can mitigate degradation,[20–23] they do not overcome the problem of short *in vivo* residence times. Consequently, a delivery platform capable of simultaneously preserving structural integrity and ensuring prolonged localized retention is essential to fully harness the power of DNA nanotechnology.

Hydrogels offer a promising solution by providing a confined, biocompatible microenvironment that stabilizes DNA nanostructures while enabling tunable release. One prevalent approach involves DNA hydrogels, assembled through canonical or non-canonical base-pairing interactions.[24] While intrinsically programmable, these matrices face inherent limitations, including high production cost and nuclease susceptibility. More critically, the mechanical strength and degradation rates of DNA hydrogels are inherently linked to the DNA network itself, limiting independent control over material properties.[25,26]

Polymer-based hydrogels represent an alternative strategy. For example, Segura and colleagues encapsulated DNA/poly-ethylenimine (PEI) polyplexes in hyaluronic acid (HA) and fibrin hydrogels to achieve localized gene delivery.[27] While this approach offers broader mechanical tunability, the use of cationic polymers like PEI raises cytotoxicity concerns. Furthermore, prior efforts have largely focused on simple oligonucleotides or DNA assemblies, rather than structurally dense, rigid DNA origami.[23,27,28] The encapsulation of such multi-helical 3D nanostructures within degradable polymeric hydrogels remains underexplored, particularly regarding how the physical confinement of the hydrogel mesh preserves their structural integrity while simultaneously acting as a localized depot to prevent rapid systemic clearance.

In this context, we developed a platform where DNA origami nanostructures function as discrete nanoparticles, effectively decoupled from the mechanical properties of the surrounding matrix. We report a biodegradable hydrogel system constructed from a composite network of thiolated HA and gelatin, engineered to encapsulate structurally dense square-block DNA nanostructures (SQBs). By systematically modulating polymer concentration, crosslinking density, and gelatin content, we tuned the hydrogel mesh size and degradation kinetics to regulate SQB release. This approach directly addresses the limitation of short residence times by providing a tunable release rate that can be tailored to specific therapeutic needs. We demonstrate that this SQB–hydrogel hybrid preserves the structural fidelity of the DNA nanostructures, enables prolonged cellular delivery *in vitro*, and markedly extends *in vivo* retention compared to free SQBs, effectively overcoming the rapid clearance hurdle. Collectively, these findings present a robust, tunable framework that overcomes key stability and delivery hurdles, paving the way for the advanced biomedical applications of complex DNA nanostructures.

2. Experimental methods

2.1. Preparation of DNA nanostructures

2.1.1. SQB folding. The p8634 scaffold, derived from the M13 genome, was prepared according to a previously established method.[5] Endotoxins were removed using 2% Triton X-114 (Sigma-Aldrich). The purified scaffold was mixed with a 5-fold molar excess of staple strands (IDT), including modified strands bearing handle sequences for subsequent Cy5.5 fluorescent dye conjugation. To assemble the SQBs, the mixture was heated at 80 °C for 15 minutes to denature the DNA strands, followed by controlled cooling from 50 °C to 40 °C at a rate of −0.1 °C per 10 minutes and 48 seconds in TE-Mg^{2+} buffer (10 mM Tris, 1 mM EDTA and 12 mM MgCl$_2$). Excess staple strands were removed *via* PEG precipitation as previously described.[5] Briefly, the SQB solution was mixed with a 20% PEG solution supplemented with 10 mM MgCl$_2$, and purified SQBs were recovered by sequential centrifugation. The successful synthesis of SQBs was verified *via* agarose gel electrophoresis and transmission electron microscopy (TEM).

2.1.2. Conjugation of Cy5.5 fluorescent dye to ssDNA and SQB. Single-stranded DNAs (ssDNAs) with a 5′-terminal amine modification were used for Cy5.5 dye conjugation. Specific sequences designed to hybridize with the SQB were conjugated with Cy5.5 using an *N*-hydroxysuccinimide (NHS) ester chemistry. Briefly, the amine-modified ssDNAs were reacted with Cy5.5-NHS (BioActs) at a molar ratio of 1:10 in DEPC-treated water (Biosesang) and incubated overnight at room temperature with shaking at 600 rpm. Following the reaction, Cy5.5-labeled ssDNAs (Cy5.5-ssDNAs) were purified by ethanol precipitation. Cold 100% ethanol (2.5 × volume, Sigma Aldrich) and 3 M sodium acetate (0.1 × volume, pH 5.2, Sigma-Aldrich) were added to the reaction mixture, followed by incubation at −20 °C for 1 hour. The mixture was centrifuged at 16 000 × g for 20 minutes at 4 °C. The supernatant was carefully removed, and the pellet was washed with 75% ethanol, followed by centrifugation under the same conditions. The pellet was dried and resuspended in 1 × TE buffer (Biosesang). To conjugate Cy5.5 to the DNA nanostructure, SQBs were annealed with a 5-fold molar excess of Cy5.5-ssDNAs relative to the handle

strands. The mixture was incubated at 37 °C for 2 hours to allow hybridization. Unbound Cy5.5-ssDNAs were subsequently removed by PEG precipitation, and the conjugation of Cy5.5 to the SQBs was confirmed by agarose gel electrophoresis.

2.1.3. K_{10}-PEG coating of SQBs. SQBs were coated with K_{10}-PEG_{5k} (Alamanda Polymers) prior to hydrogel encapsulation, *in vitro* serum stability assays, *in vitro* cellular uptake, and *in vivo* retention tests.[22] K_{10}-PEG_{5k} and SQBs were mixed at an N : P ratio of 1 : 1, corresponding to the molar ratio of amine-derived nitrogen to DNA phosphate groups. The mixture was incubated at room temperature for 1 hour to ensure complete coating.

2.2. Characterization of DNA nanostructure

2.2.1. Removal of K_{10}-PEG coating from SQB. The K_{10}-PEG coating was removed using chondroitin sulfate as a competitive polyanion. Chondroitin sulfate was added at a 100-fold molar excess relative to the amine groups on the oligolysine (K_{10}) in the K_{10}-PEG coating. The sample was incubated at 37 °C for 2 hours to induce electrostatic binding between the negatively charged chondroitin sulfate and the positively charged oligolysine (K_{10}) domain. This interaction displaced the K_{10}-PEG coating from the DNA nanostructure surface, yielding de-coated SQBs suitable for further analysis.

2.2.2. Agarose gel electrophoresis analysis. The structural integrity and electrophoretic mobility of the DNA nanostructures were assessed using 1.5% agarose gel electrophoresis. Gels were prepared using $0.5 \times$ TBE buffer supplemented with 10 mM $MgCl_2$, and electrophoresis was performed in the same buffer system to preserve the folded structure. Samples were mixed with $6 \times$ DNA loading dye (Enzymonics), and 10 μL of each sample was loaded per well. Electrophoresis was performed at 70 V for 50 minutes at room temperature, and DNA bands were visualized using an Invitrogen™ iBright™ CL750 Imaging System (Thermo Fisher Scientific).

2.2.3. TEM analysis. For TEM analysis, distinct bands corresponding to SQBs were excised from agarose gel under UV illumination. The gel slices were crushed and placed into DNA gel extraction spin columns (Bio-Rad), and the SQBs were recovered by centrifugation at $13\,000 \times g$ for 5 minutes. Prior to sample application, CF200-Cu grids (Electron Microscopy Sciences) were glow-discharged. For negative-stain TEM imaging, 4 μL of SQB solution (1–5 nM in $1 \times$ TE buffer containing 10 mM $MgCl_2$) was applied to the grids and incubated for 1 minute at room temperature. Excess solution was gently removed using filter paper. The grids were then stained with 4 μL of 0.75% aqueous uranyl formate for 1 minute, followed by gentle removal of excess stain. Grids were protected from light and air-dried overnight. Images were acquired using a JEOL JEM-1400 transmission electron microscope operated at 80 kV.

2.3. Stability test of K_{10}-PEG-coated SQB in serum

To assess structural integrity, K_{10}-PEG-coated SQBs (10 nM) were incubated in serum-containing culture medium at 37 °C for up to 10 days. At designated time points (day 1, 3, 7, and 10), samples were collected for analysis. Nuclease activity was quenched by addition with 5 mM ethylene glycol-bis(2-amino-ethylether)-*N*,*N*,*N*′,*N*′-tetraacetic acid (EGTA, Biosesang) and 10% β-mercaptoethanol (Sigma-Aldrich), followed by incubation at 37 °C for 30 minutes. The K_{10}-PEG layer was then removed using chondroitin sulfate as described in Section 2.2.1, and the stability of the recovered SQBs was verified *via* agarose gel electrophoresis.

2.4. Preparation and characterization of SQB-hydrogel hybrids

2.4.1. Synthesis of thiolated hyaluronic acid (HA-SH). HA-SH with 77.4% degree of substitution (DS) was synthesized using 200 kDa sodium hyaluronate (Lifecore Biomedical, USA), dithiodipropionic dihydrazide (DTP, Sigma Aldrich), 1-ethyl-3-(3-dimethylaminopropyl)-carbodiimide (EDC, Sigma Aldrich), and dithiothreitol (DTT, Sigma Aldrich) using EDC-activated coupling.[29] In short, HA was dissolved in water and sparged with nitrogen. DTP (1.34 mole equivalents) was added and stirred thoroughly. The pH of the mixture was maintained at 4.75 by adding 1 N HCl. EDC (2.1 mole equivalents) was then added, and the reaction was conducted for 4 hours at pH 4.75 under nitrogen atmosphere. 1 N NaOH was added to stop the reaction, raising the pH to 7.0. Then, the addition of DTT (13 equivalents with respect to the HA disaccharide unit) was done and stirred for 24 hours to completely reduce the disulfide bonds under nitrogen condition. The solution was then subjected to dialysis (RC Dialysis Membrane Tubing 6–8 kDa MWCO, Thermofisher Scientific) for 72 hours against dilute HCl (pH 3.5) containing 100 mM NaCl. Then, additional dialysis was performed against diluted HCl at pH 3.5 for 48 hours. Then, the solution was centrifuged to remove insoluble byproducts and the supernatant was lyophilized. The lyophilized product was then characterized using H-NMR to determine its %DS as described in Fig. S1. In brief, compared to the N-acetyl methyl signal of HA at $\delta 1.9182$, HA-SH displayed new resonances at $\delta 2.6171$ and $\delta 2.7$, corresponding to the side-chain methylene protons (CH_2CH_2SH) (Fig. S1). The degree of substitution (%DS) was calculated by integrating the DTP methylene signals relative to the N-acetyl methyl peak, yielding a %DS of 77.46% (Fig. S1).

2.4.2. Formulation and physiochemical characterization of SQB-hydrogel hybrids. Four formulations of SQB-hydrogel hybrids were prepared using varying concentrations of three backbone components: 4-Arm-5KPEG-Maleimide (Advanced BioChemicals), synthesized HA-SH (77.4% DS), and gelatin from bovine skin (Sigma Aldrich). These three major backbone components are varied in concentrations to modulate the mesh size of the hydrogel as well as the degradation profile as shown in Table 1.

The formulated hydrogels exhibit varying degrees of polymer crowding, crosslinking density, and gelatin content, which together affected mesh size, degradation, consequently affecting the release profile of encapsulated nanostructures. For example, crosslinking density was varied between H.Mal-H.HA (100% crosslinked) and L.Mal-H.HA group (50% crosslinked), while polymer density was varied between the high PEG-Maleimide

Table 1 Formulation recipe of four different types of gels in 200 μL of hydrogel

Type of gels	4-armPEG-Maleimide [mM]	5 wt% HA-SH to 5 wt% Gelatin [volume ratio]
High PEG-Maleimide High HA (H.Mal-H.HA)	High: 26.6 mM (excess maleimide for –SH)	3-to-1
High PEG-Maleimide Low HA (H.Mal-L.HA)	High: 26.6 mM (excess maleimide for –SH)	1-to-1
Low PEG-Maleimide High HA (L.Mal-H.HA)	Low: 13.3 mM	3-to-1
Low PEG-Maleimide Low HA (L.Mal-L.HA)	Low: 13.3 mM	1-to-1

gels (H.Mal-H.HA and H.Mal-L.HA) and the low PEG-Maleimide gels (L.Mal-H.HA and L.Mal-L.HA). In-house synthesized and oligosaccharide K_{10}-PEG-coated SQB was each formulated into these hydrogels (10 nM per hydrogel), as well as $MgCl_2$ solution (10 mM). Hydrogel gelation is done by simply thoroughly mixing all components.

To evaluate the mechanical and rheological properties of the hydrogels, the oscillatory rheological measurements were performed using a rheometer (MCR102, Anton Paar, Graz). Strain sweep tests were first conducted over a strain range of 0.1 to 500% to identify the linear viscoelastic (LVE) regime for each hydrogel formulation. Stiffness was quantified as a storage modulus (G') obtained from the plateau region within the LVE regime. Subsequently, frequency sweep measurements were performed at a fixed strain within the LVE region to confirm stable linear viscoelastic behavior across the tested frequency range (Fig. S2). Then, swelling behavior was evaluated using a gravimetric method. Each hydrogel sample was incubated for 3 days at room temperature for complete swelling. The swelling ratio was calculated as follows:

$$\text{Swelling ratio } (\%) = \frac{M_w - M_d}{M_d} \times 100$$

where M_w and M_d represent the wet mass (g) and dry mass (g), respectively.

To investigate the mesh size distributions of the hydrogels, prepared hydrogels were fully swollen in 1 × PBS at 37 °C for 24 hours and lyophilized. Samples were then sputter-coated with platinum (Pt) for 30 seconds at 15 mA. The surface morphology was imaged using field-emission scanning electron microscopy (FE-SEM; Nova-SEM, FEI). Additionally, elemental analysis was performed using energy-dispersive X-ray spectroscopy (EDS) to verify the retention of magnesium ions (Mg^{2+}) within the hydrogel matrix. SEM images were analyzed using Fiji-ImageJ software.

2.4.3. Recovery of SQBs from hydrogels. To analyze the structural integrity of encapsulated SQBs, the hydrogels were enzymatically degraded. The gels were mechanically ground and treated with a mixture of collagenase type I (200 U, Sigma Aldrich), hyaluronidase (400 U, Sigma Aldrich), and 100 mM DTT (Sigma Aldrich) for 20 minutes at 37 °C. Following complete dissociation, the recovered SQBs were purified for further analysis.

2.5. *In vitro* studies of SQB-hydrogel hybrids

2.5.1. Release study. The stability and release behavior of SQB-loaded hydrogels were evaluated in 48-well flat-bottom plates (Sarstedt). To assess the contribution of diffusion and temperature-induced gelatin dissociation, hydrogels were incubated in phenol red-free medium or in 1 × PBS containing 10 mM $MgCl_2$ at 4 °C and 37 °C. For enzyme-mediated degradation, hydrogels were incubated in 1 × PBS containing 10 mM $MgCl_2$, collagenase I (10 U/500 μL), and hyaluronidase (20 U/500 μL) at 37 °C. At predetermined time points (days 1, 3, and 7), supernatants were collected and replaced with fresh buffer (with or without enzymes), and the remaining hydrogels were retained for subsequent analysis. The collected supernatants were analyzed via agarose gel electrophoresis, and the retained hydrogels were quantified for Cy5.5 fluorescence using an iBright FL1000 Imaging System (Thermo Fisher Scientific) and a GloMax Discover System (Promega).

2.5.2. Analysis for encapsulated and released SQBs. Following enzymatic dissociation, the SQB-containing solution was concentrated using Amicon Ultra-0.5 mL 100 kDa centrifugal filter units (Merck Millipore). The enzyme-digested sample was then loaded and centrifuged at 14 000 × g for 10 minutes. The concentrated SQB solution was recovered by inverted centrifugation at 1000 × g for 2 minutes. Recovered SQBs were treated with chondroitin sulfate to remove the K_{10}-PEG coating prior to 1.5% agarose gel electrophoresis and TEM analysis. To quantify SQB release, Cy5.5 fluorescence images were processed using Fiji (NIH, USA). The hydrogel region was defined as the region of interest (ROI), and the mean fluorescence intensity was measured. The percentage of released SQBs was calculated as follows:

$$\%\text{Release}_t = 100 - \%\text{Remaining}_t = \left(1 - \frac{I_t}{I_0}\right) \times 100$$

where I_t is the mean ROI intensity at time t, and I_0 is the mean ROI intensity at day 0.

2.5.3. Cellular uptake study. RAW264.7 cells were seeded in a 24-well plate at a density of 5×10^4 cells per well. Cells were treated with 50 μL of either SQBs or SQB–hydrogels (containing 10 nM SQBs). Hydrogels were placed in Transwell insert (Corning®, pore size: 0.4 μm) to allow diffusion-mediated delivery without direct cell contact. After 1 hour, the medium was replaced. At designated time points (days 1, 3, and 5), cells were washed with PBS and imaged using a fluorescence microscope. Intracellular fluorescence intensity was quantified using ImageJ software.

2.6. *In vivo* studies of SQB-hydrogel hybrids

2.6.1. *In vivo* fluorescence imaging of implanted gels. The *in vivo* retention of SQB-Cy5.5 were assessed in healthy

C57/BL/6 mice. All animal experiments were performed in accordance with the Guidelines for Care and Use of Laboratory Animals of the Korea Institute of Science and Technology (KIST) and approved by the Institutional Animal Care Use Committees (IACUC) of KIST. The dorsal region of the mice was shaved, and four types of SQB-loaded hydrogels (100 nM SQB, 50 μL per gel) were subcutaneously implanted at two or three sites per mouse. As a positive control, 50 μL of free SQB (10 nM in 1 × PBS) was injected subcutaneously. Untreated sites served as negative controls. On day 0, 3, and 7 post-implantation, fluorescence intensity was imaged using an IVIS Lumina Series III system (PerkinElmer) and quantified using the Living Image® 4.4 software (PerkinElmer).

2.6.2. Histological analysis of explanted tissue. Mice were sacrificed on day 10 post-implantation. Skin tissues containing the hydrogels were excised, fixed in 4% paraformaldehyde (Sigma Aldrich) for 30 minutes, and cryoprotected in 30% sucrose solution for 3 days. Tissues were embedded in OCT compounds, frozen at −80 °C, and cryosectioned at a thickness of 10 μm (Leica CM1860, Leica Biosystems). Sections were washed to remove OCT and mounted with VECTASHIELD® Antifade Mounting Medium with DAPI (Vector Laboratories). Fluorescence images were acquired using an upright microscope (Eclipse Ts2R, Nikon) and analyzed using Fiji-ImageJ software.

2.7. Statistical analysis

All quantitative data are presented as mean ± standard deviation (SD). Statistical significance was assessed using one-way analysis of variance (ANOVA) followed by Tukey's multiple comparisons test. A *p*-value of less than 0.05 was considered statistically significant (*$p < 0.05$, **$p < 0.01$, ***$p < 0.001$, and ****$p < 0.0001$). All statistical analyses were performed using GraphPad Prism software.

3. Results and discussion

3.1. Preparation and characterization of SQBs

To study hydrogel-mediated sustained delivery while ensuring the structural preservation of DNA nanostructures against physiological challenges, we selected the square-block DNA origami (SQB) as a representative, structurally dense DNA nanoparticle model. The SQB was designed as a compact block-shaped nanostructure (approximately 27 × 35 × 22.5 nm) using the p8634 single-stranded DNA scaffold and a defined set of staple strands (Fig. 1A), as previously described.[5,30] Each SQB was labeled with ten Cy5.5 fluorophores to enable precise optical tracking.

To verify the stepwise formation, agarose gel electrophoresis compared samples from each assembly stage (Fig. 1B). The p8634 scaffold migrated as a single, distinct band. Notably, the scaffold-staple mixture displayed a retarded electrophoretic mobility compared to the scaffold alone, indicative of partial hybridization even prior to thermal annealing. Following annealing, the assembled SQBs appeared as a predominant band, accompanied by a faint higher-molecular-weight species

consistent with a minor dimer-like population. Subsequent PEG precipitation effectively removed excess staple strands and free Cy5.5 labels, as evidenced by the well-resolved bands across both nucleic acid and Cy5.5 fluorescence channels. Corroborating these electrophoretic profiles, TEM imaging revealed structurally homogeneous SQBs with dimensions closely matching the *in silico* design (Fig. 1C). These combined analyses validate the successful assembly, high monodispersity, and structural integrity of the SQBs prior to hydrogel encapsulation.

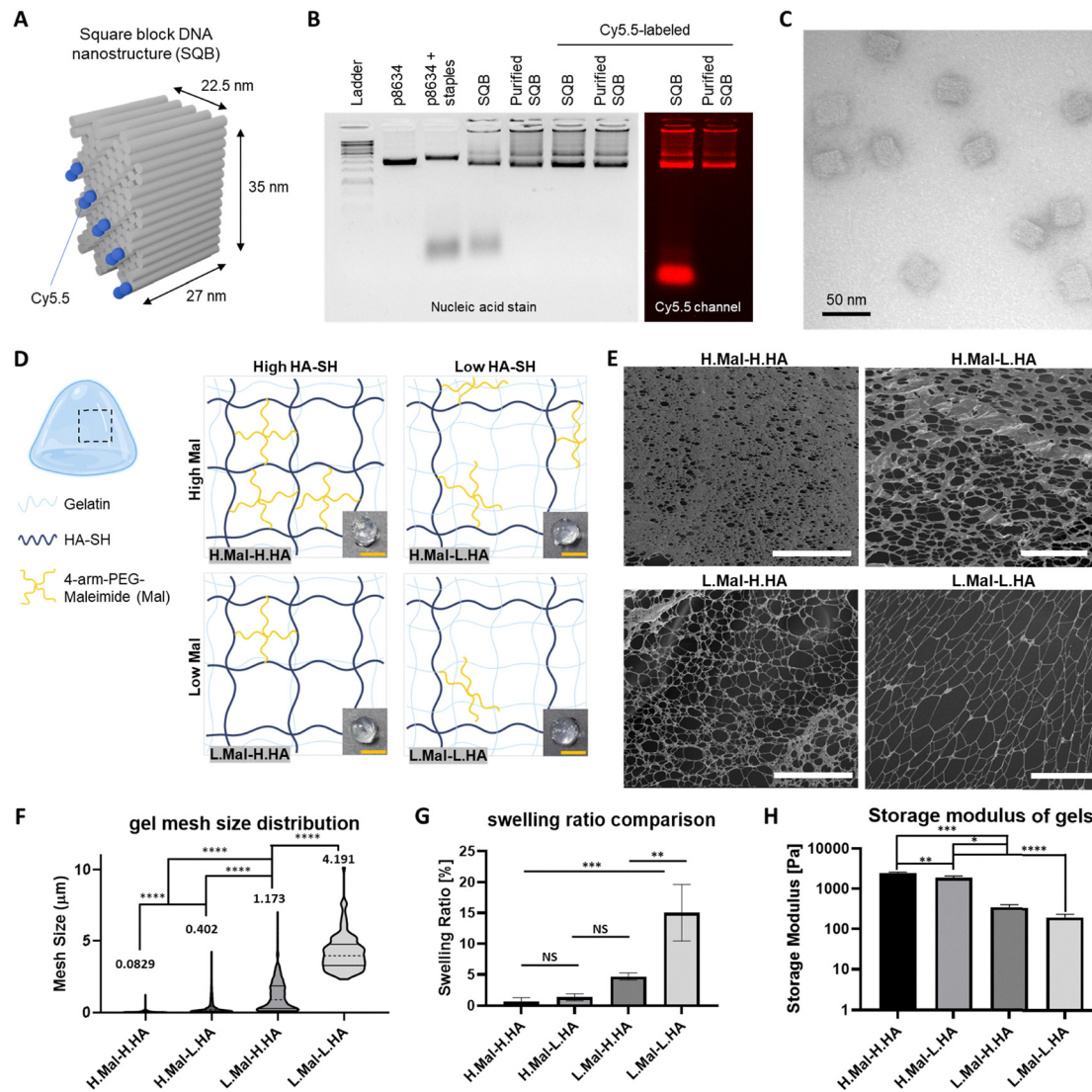### 3.2. Fabrication and characterization of HA/gelatin hydrogels

Hydrogels were engineered with varying polymer compositions to systematically modulate crosslinking density and gelatin content. These parameters govern mesh size and degradation kinetics, which are essential for regulating the release and long-term stability of encapsulated SQBs to address the challenge of short *in vivo* residence times. The matrix comprised thiolated HA (HA-SH), type B gelatin, and a 4-arm PEG-maleimide crosslinker. These biocompatible components not only allow for tunable mechanical properties but also present abundant functional groups (carboxylic, hydroxyl, and amine) that create a favorable microenvironment for DNA nanostructures.

The hydrogels were formed through a dual-crosslinking strategy (Fig. 1D): (i) rapid covalent crosslinking between HA-SH and maleimide, establishing the primary elastic network, and (ii) physical reinforcement through the thermal gelation of gelatin at low temperatures. Importantly, while the gelatin component undergoes thermal softening and gradual dissociation at physiological temperature (37 °C), the covalently cross-linked HA network ensures the overall structural integrity of the localized depot. We formulated four hydrogels designated based on their relative concentrations of maleimide crosslinker (Mal) and hyaluronic acid (HA): High Mal-High HA (H.Mal-H.HA), High Mal-Low HA (H.Mal-L.HA), Low Mal-High HA (L.Mal-H.HA), and Low Mal-Low HA (L.Mal-L.HA). All formulations formed transparent, homogeneous gels within 20 seconds, with uniform dye distribution confirming efficient component mixing (Fig. S2A).

Scanning electron microscopy (SEM) elucidated the impact of composition on network topology (Fig. 1E). The H.Mal-H.HA formulation, possessing the highest crosslinking density, exhibited a dense structure with the smallest average mesh size (0.083 μm) (Fig. 1F). Conversely, L.Mal-L.HA displayed a highly porous structure (mesh size: 4.191 μm). The H.Mal-L.HA and L.Mal-H.HA showed mesh sizes of 0.402 μm and 1.173 μm, respectively. These structural variations are directly governed by the crosslinking chemistry, where higher maleimide/thiol concentrations densify the covalent network. Although these mesh sizes are larger than individual SQB dimensions, the physical confinement and tortuosity of the dense covalent network are expected to significantly impede the diffusion of the DNA nanostructures.

To further evaluate network porosity, we measured swelling ratios (Fig. 1G). The L.Mal-L.HA hydrogel, characterized by the largest mesh size, exhibited the highest swelling ratio of

Fig. 1 Preparation and characterization of square block DNA nanostructures (SQBs) and hydrogels. (A) Schematic illustration of the SQB, designed as a compact block-shaped DNA origami structure functionalized with ten Cy5.5 fluorophores on one face. (B) Agarose gel electrophoresis showing the p8634 scaffold, the scaffold−staple mixture prior to thermal annealing, the folded SQBs, and SQBs purified by PEG precipitation. Nucleic acid−stained and Cy5.5 fluorescence channels are shown, confirming the folded SQBs as a predominant band and the effective removal of excess staple strands after PEG purification. (C) Transmission electron microscopy (TEM) image of SQBs showing well-defined square block morphology with dimensions consistent with the designed geometry. (D) Schematics describing the design of four hydrogels targeting distinct degradation profiles, alongside photographs of the crosslinked gels. (E) Representative scanning electron microscopy (SEM) images of each hydrogel formulation, revealing differences in surface mesh structure. Scale bars: 10 μm. (F) Quantitative analysis of gel mesh size distribution based on SEM images. (G) Quantification of the swelling ratio of the hydrogels. (H) Rheological analysis showing the average storage modulus (G') of the crosslinked hydrogels. Data represent mean ± SD (n = 3). Statistical significance was evaluated using one-way ANOVA (*$p < 0.05$, **$p < 0.01$, ***$p < 0.001$, ****$p < 0.0001$).

approximately 15%, whereas the other three formulations maintained swelling ratios below 5%. This finding is consistent with the SEM observations, as looser networks with larger mesh sizes permit greater water uptake.

Mechanical characterization further corroborated these trends. Stiffness values (storage modulus, G') determined within the linear viscoelastic (LVE) regime (Fig. 1H and Fig. S2B) confirmed that H.Mal-H.HA and H.Mal-L.HA possessed robust mechanical strength (2471 Pa and 1876 Pa, respectively), whereas the less crosslinked L.Mal-H.HA and L.Mal-L.HA were significantly softer (350 Pa and 200 Pa, respectively). These results

confirm that matrix stiffness and porosity can be precisely tuned independent of the encapsulated nanoparticles, establishing a versatile library of hydrogels capable of providing programmable release profiles.[31,32]

3.3. Characterization and stability assessment of K_{10}-PEG-coated SQBs

To ensure the stability of SQBs within the enzymatically active hydrogel microenvironment, we introduced a protective polymer layer by coating the nanostructures with a K_{10}-PEG$_{5k}$ polymer via electrostatic interaction (Fig. 2A), as described in
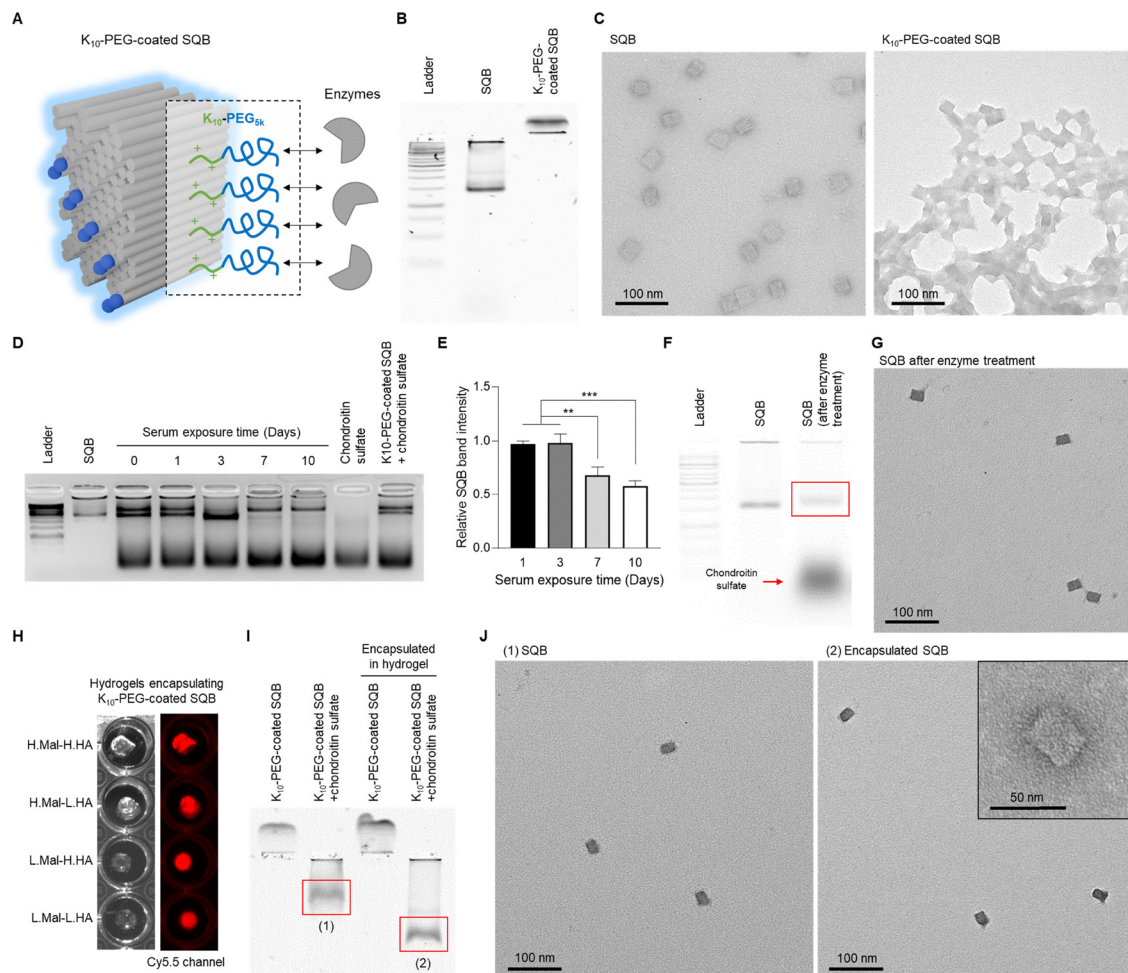
Fig. 2 Characterization of K_{10}-PEG-coated SQBs and their structural stability before and after hydrogel encapsulation. (A) Schematic illustration of K10-PEG-coated SQBs. SQBs were coated with a K_{10}-PEG$_{5k}$ polymer *via* electrostatic interaction to enhance resistance to enzymatic degradation and reduce nonspecific interactions with hydrogel components. Characterization of K_{10}-PEG-coated SQBs. (B) Agarose gel electrophoresis of SQBs before and after K_{10}-PEG coating. Charge neutralization by the oligolysine domain results in substantially reduced electrophoretic mobility. (C) TEM images of uncoated and K_{10}-PEG-coated SQBs. Coated SQBs retain their square-block morphology but display a blurred outer boundary consistent with the presence of the polymer layer; mild aggregation is observed. Scale bars: 100 nm. Stability of K_{10}-PEG-coated SQBs in serum-containing medium at 37 °C. (D) Agarose gel electrophoresis of SQBs incubated for up to 10 days; coating was removed using chondroitin sulfate prior to electrophoresis. (E) Quantification of SQB band intensities from (D), normalized to day 0. K_{10}-PEG coating preserved SQB integrity for at least 3 days, with gradual decreases to 68% and 58% on days 7 and 10. Data represent mean ± SD ($n = 3$). One-way ANOVA with Tukey's *post hoc* test (**$p < 0.01$, ***$p < 0.001$). Effect of matrix-degrading enzymes on K_{10}-PEG-coated SQBs. (F) Agarose gel electrophoresis after treatment with collagenase I and hyaluronidase. Coating was removed prior to electrophoresis. The slight band shift (red box) reflects changes in surface properties due to enzyme interactions or residual coating materials, rather than structural degradation. The red arrow indicates the chondroitin sulfate band. (G) TEM images of SQBs extracted from the red-boxed bands in (F). The recovered nanostructures retain their square-block morphology, confirming structural integrity after exposure to collagenase I and hyaluronidase. Scale bar: 100 nm. (H) Bright-field (left) and Cy5.5 fluorescence (right) images of four HA/gelatin hydrogels supplemented with 10 mM Mg^{2+} and loaded with K_{10}-PEG-coated, Cy5.5-labeled SQBs. Homogeneous fluorescence throughout the matrices indicates successful encapsulation and uniform dispersion of the nanostructures. Structural integrity of SQBs before and after hydrogel encapsulation and recovery. (I) Agarose gel electrophoresis comparing SQBs before (red box 1) and after (red box 2) hydrogel encapsulation and enzymatic recovery. The K_{10}-PEG coating was removed prior to electrophoresis. The observed mobility shift is attributed to residual hydrogel components adhering to the nanostructures. (J) TEM images of SQBs extracted from the red-boxed bands in (I). SQBs recovered after hydrogel encapsulation and enzymatic digestion maintain morphology comparable to pre-encapsulation controls. The inset shows an enlarged view with dimensions consistent with the designed SQB geometry. Scale bars: 100 nm; inset: 50 nm.

a previous study.[22] This K_{10}-PEG coating strategy is designed to shield DNA nanostructures from nuclease-induced degradation and minimize nonspecific binding to hydrogel components. Successful coating was confirmed by both agarose gel electrophoretic and microscopic analyses. In agarose gel electrophoresis, K_{10}-PEG-coated SQBs exhibited markedly reduced mobility

compared to uncoated controls due to charge neutralization by the oligolysine domain (Fig. 2B). TEM imaging further revealed that the coated SQBs preserved their characteristic square-block geometry while displaying a diffuse polymer corona around the DNA core, distinct from the sharp edges of uncoated SQBs (Fig. 2C). This confirms that the K_{10}-PEG$_{5k}$

polymer effectively coats the nanostructure without compromising its structural integrity.

We next assessed the stability of K_{10}-PEG coated SQBs under biologically relevant conditions. K_{10}-PEG-coated SQBs (10 nM) were incubated in serum-containing medium (10%) at 37 °C for up to 10 days. After removing the coating with chondroitin sulfate, agarose gel electrophoresis revealed that SQBs remained intact for at least 3 days, followed by a gradual decrease in band intensity to 68 ± 0.07% and 58 ± 0.05% on days 7 and 10, respectively (Fig. 2D and E). More importantly, given that SQBs encapsulated within hydrogels are eventually exposed to matrix-degrading enzymes during release, we examined their stability in the presence of collagenase I and hyaluronidase. K_{10}-PEG-coated SQBs were incubated with both enzymes for 2 hours at 37 °C, after which the coating was removed to directly assess DNA nanostructure integrity. Even under these degradative conditions, intact SQB bands remained visible by agarose gel electrophoresis (Fig. 2F). While an electrophoretic mobility shift was observed, this is attributable to nonspecific enzyme adsorption or residual K_{10}-PEG coating layers rather than structural disassembly. TEM imaging of the corresponding recovered bands confirmed that the nanostructures regained sharply defined boundaries, indistinguishable from pristine SQBs (Fig. 2G). This finding confirms that the core DNA architecture remained structurally intact throughout both the coating process and exposure to the enzymatic milieu required for hydrogel erosion.

3.4. Encapsulation and post-recovery structural integrity of SQBs

We evaluated the encapsulation efficiency and spatial distribution of SQBs within the hydrogel matrix. Fluorescence microscopy of hydrogels loaded with Cy5.5-labeled, K_{10}-PEG-coated SQBs revealed a homogeneous signal throughout the construct, indicating uniform dispersion without aggregation (Fig. 2H). Notably, scanning electron microscopy–energy-dispersive X-ray spectroscopy (SEM-EDS) analysis confirmed the retention of Mg^{2+} ions within the hydrogel network (Fig. S3). This ionic microenvironment is essential for maintaining the structural fidelity of DNA nanostructures,[33,34] suggesting the HA/gelatin matrix functions as a stabilizing reservoir.

To assess the structural integrity of SQBs following the complete cycle of encapsulation and release, we recovered the nanostructures by enzymatically degrading the hydrogel with collagenase I and hyaluronidase. After removing the K_{10}-PEG coating, agarose gel electrophoresis showed that the recovered SQBs (Lane 4) maintained electrophoretic profiles comparable to those of pristine SQBs (Lane 2), appearing as a distinct single band (Fig. 2I). Although a noticeable mobility shift was observed, this is attributable to the presence of residual hydrogel-derived impurities. Importantly, TEM imaging of the extracted bands confirmed that the square-block geometry was fully preserved, with dimensions closely matching the in silico SQB design (Fig. 2J).

Collectively, these results demonstrate that the proposed hydrogel platform accommodates DNA nanostructures without

structural damage and preserves their integrity throughout the entire process of encapsulation, storage, and enzymatic release.

3.5. Sustained release mechanism of SQBs from hydrogels

To elucidate how hydrogel composition and matrix-remodeling pathways govern SQB release, we evaluated the retention and release profiles of K_{10}-PEG-coated, Cy5.5-labeled SQBs from four hydrogel formulations. Experiments were conducted over 7 days under three controlled conditions designed to isolate the contributions of (i) diffusion through an intact network, (ii) thermally induced gelatin dissociation, and (iii) enzymatic matrix degradation. First, under diffusion-only conditions at 4 °C (Fig. 3A, left), the hydrogel network remained structurally stable. Consequently, cumulative release remained low across all formulations, staying below 30% by 7 days (Fig. 3B, left). These results indicate that an intact network effectively restricts SQB mobility when thermal and enzymatic fluctuations are minimized.

At 37 °C in absence of enzymes (Fig. 3A, middle), release rates increased as the gelatin component underwent thermal softening, which enlarges the effective mesh size. The more porous formulations, H.Mal-L.HA and L.Mal-L.HA, exhibited approximately 50% release by day 7, whereas the most densely crosslinked hydrogel, H.Mal-H.HA, released only 25% (Fig. 3B, middle). These release profiles are directly corroborated by agarose gel electrophoresis of the collected supernatants (Fig. S4A), where intact SQB bands were markedly prominent in the loosely crosslinked samples (e.g., L.Mal-H.HA and L.Mal-L.HA) compared to the denser formulations, providing visual evidence of the accelerated release kinetics driven by thermal softening. Importantly, while gelatin undergoes thermal softening at physiological temperature, the covalently crosslinked HA network preserves the structural integrity of the localized depot, effectively preventing premature burst release. This mechanism is supported by gradual bulk shrinkage due to the outward diffusion of uncrosslinked gelatin; H.Mal-H.HA retained 93.7% of its volume after 10 days, whereas L.Mal-L.HA retained only 67.7% (Fig. S4B).

Finally, enzyme-mediated degradation at 37 °C triggered the most rapid release (Fig. 3A, right). By day 3, cumulative release ranged from 52% (H.Mal-H.HA) to 75% (L.Mal-L.HA), increasing further to 57% and 92%, respectively, by day 7 (Fig. 3B, right). This accelerated release profile correlated with rheological measurements, where storage modulus (G') of enzyme-treated hydrogels decreased markedly over time (Fig. 3C). Regardless of crosslinking density, all formations underwent significant mechanical degradation, confirming substantial matrix erosion. Collectively, these findings demonstrate that SQB release is governed by the cooperative interplay of restricted diffusion, thermal gelatin softening, and enzymatic degradation. We conceptualized this mechanism in Fig. 3D, which illustrates that denser networks (e.g., H.Mal-H.HA) erode more slowly and retain SQBs longer, whereas loosely crosslinked matrices (e.g., L.Mal-L.HA) degrade rapidly.

3.6. Hydrogel-mediated sustained cellular delivery of SQBs

To examine how hydrogel-driven release translates into cellular availability, RAW 264.7 macrophages were used as a representative
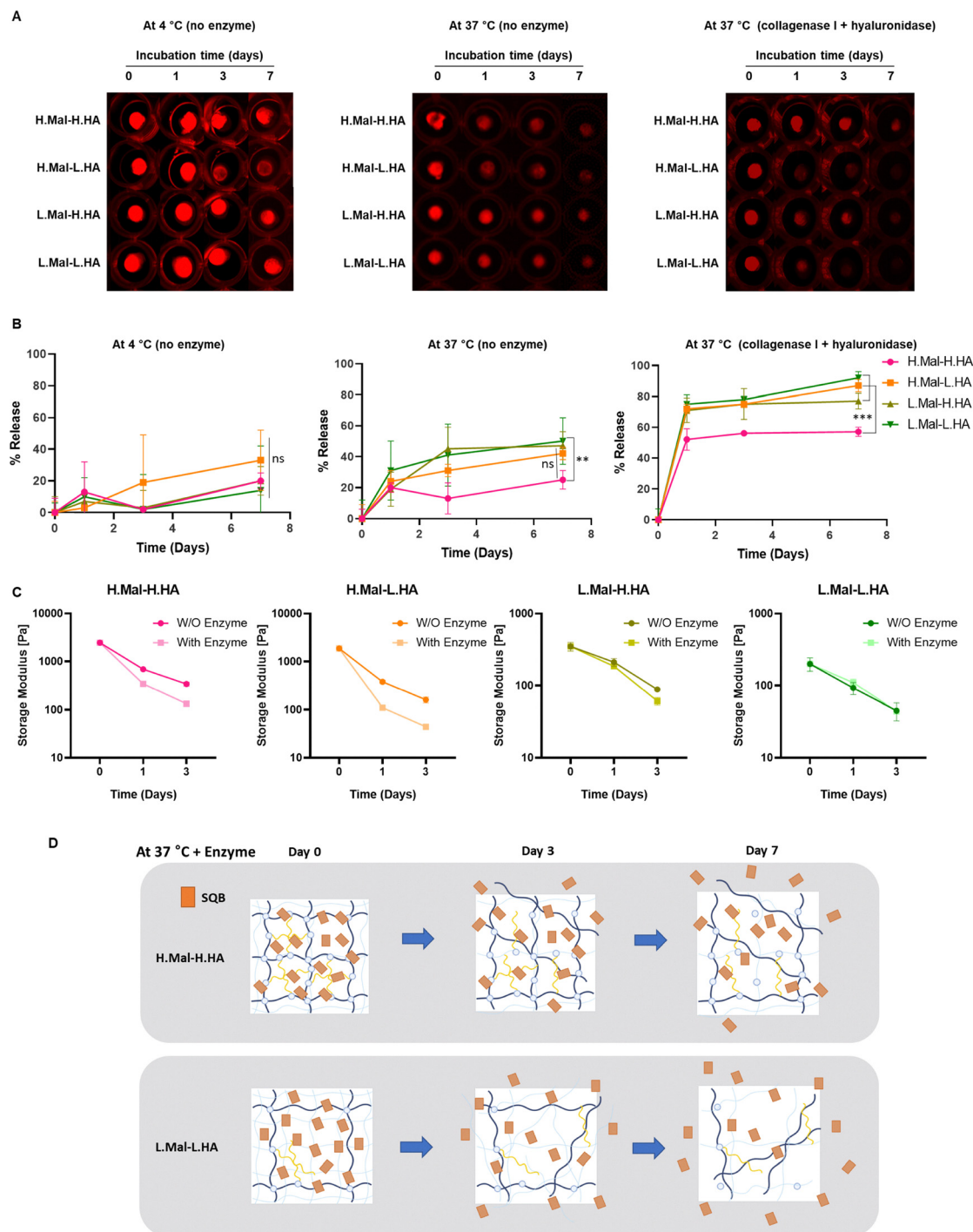
Fig. 3 Sustained release behavior of SQBs from HA/gelatin hydrogels. (A) Representative fluorescence images of four HA/gelatin hydrogel formulations (H.Mal-H.HA, H.Mal-L.HA, L.Mal-H.HA, and L.Mal-L.HA) encapsulating Cy5.5-labeled SQBs, monitored over 7 days under three conditions: diffusion-only (4 °C, no enzymes), thermal softening (37 °C, no enzymes), and enzymatic degradation (37 °C with collagenase I and hyaluronidase). Fluorescence intensity reflects the amount of SQBs retained within the gel. (B) Quantification of gel-retained Cy5.5 fluorescence for each hydrogel formulation under the three conditions shown in (A). Data represent mean $\pm$ SD (n = 3). Diffusion-only conditions resulted in minimal release across all formulations, whereas 37 °C incubation increased release in a composition-dependent manner; enzymatic treatment produced the most rapid loss of fluorescence, consistent with matrix erosion. (C) Storage modulus (G') of the four hydrogel formulations incubated at 37 °C with or without enzymes for up to 3 days. Enzymatic treatment induced a marked time-dependent decrease in G' across all formulations. While denser hydrogels exhibited larger absolute reductions in stiffness, the loosely crosslinked networks showed rapid loss of mechanical integrity, confirming progressive matrix erosion. (D) Schematic illustration summarizing SQB retention and release behavior in highly *versus* weakly crosslinked hydrogels under enzymatic degradation conditions. Dense networks resist erosion and retain SQBs longer, whereas weakly crosslinked matrices degrade rapidly, accelerating SQB release.

model with high nuclease activity. We compared the cellular uptake of free K_{10}-PEG-coated SQBs *versus* those released from the hydrogel formulations using a Transwell co-culture system, as schematically illustrated in Fig. S5A. To simulate bolus administration, cells in the free SQB group were incubated with nanostructures (10 nM) for 1 hour, followed by complete media exchange. In contrast, SQB-loaded hydrogels were sequestered in Transwell inserts to facilitate continuous, diffusion-mediated delivery without direct cell contact. Prior to analyzing uptake, we confirmed that non-treated control cells exhibited negligible fluorescence in the Cy5.5 channel from day 1 to 5, ensuring that all detected signals originated from internalized SQBs (Fig. S5B).

Fluorescence microscopy and bright-field imaging (Fig. 4A) revealed distinctly different kinetic patterns between the delivery models. The free SQB group showed a rapid surge in intracellular fluorescence at day 1, a 60-fold increase over untreated controls, indicating efficient initial endocytosis. However, the signal intensity significantly diminished by day 3 and was nearly undetectable by day 5. Quantitative analysis confirmed this transient uptake

profile (Fig. 4B), suggesting that without a continuous external supply, internalized nanostructures are rapidly cleared or degraded by intracellular nucleases.

Conversely, cells incubated with SQB-loaded hydrogels exhibited progressive intracellular accumulation, with fluorescence intensity steadily increasing over the 5-day period. Notably, the intracellular accumulation profiles closely mirrored the previously observed release kinetics; the loosely crosslinked L.Mal-L.HA formulation resulted in the highest intracellular accumulation by day 5, whereas the more densely crosslinked H.Mal-H.HA induced a slower, more gradual increase (Fig. 4B). Specifically, the L.Mal-L.HA group exhibited a 7.7-fold higher Cy5.5 signal compared to that of the densest H.Mal-H.HA hydrogel.

These results demonstrate that the hydrogel platform functions as an effective sustained-release depot. Unlike bolus administration, which is limited by rapid clearance, the hydrogel system provides a continuous supply of SQBs, thereby maintaining therapeutic intracellular concentrations over an extended duration.
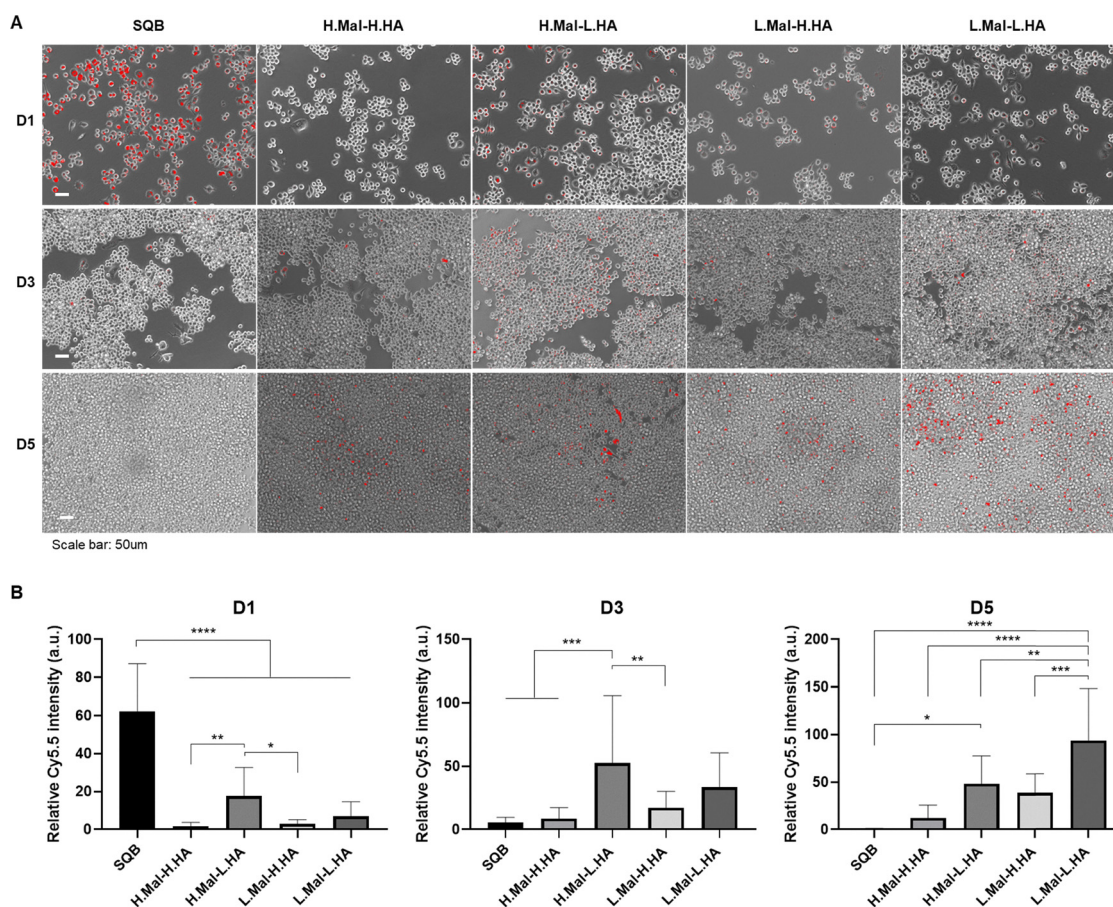
Fig. 4 Sustained intracellular delivery of SQBs enabled by hydrogel-mediated release. (A) Representative merged fluorescence and bright-field microscopy images of RAW 264.7 macrophages treated with either free SQBs or SQB−hydrogel hybrids containing Cy5.5-labeled nanostructures (red) over a 5-day period. Cells were incubated with 50 μL of 10 nM free SQBs or SQB-loaded hydrogels for 1 hour, followed by complete media exchange. For hydrogel-treated groups, Transwell inserts were used to allow diffusion-mediated delivery without direct hydrogel−cell contact. Scale bar: 50 μm. (B) Quantification of intracellular Cy5.5 fluorescence intensity in macrophages over time. Free SQBs exhibited rapid uptake at day 1 followed by a sharp decline, whereas SQB−hydrogel hybrids resulted in lower initial uptake but sustained and increasing fluorescence over time, consistent with the degradation profiles of each hydrogel. Data represent mean ± SD (n = 5−16). Statistical analysis was performed using one-way ANOVA with Tukey's *post hoc* test (*p < 0.05, **p < 0.01, ***p < 0.001, ****p < 0.0001).

3.7. *In vivo* prolonged retention of SQBs *via* hydrogel encapsulation

Encouraged by the sustained delivery observed *in vitro*, we assessed whether hydrogel encapsulation could extend the *in vivo* retention time of SQBs. Four hydrogel formulations, each encapsulating 10 nM Cy5.5-labeled SQBs, were subcutaneously implanted into the dorsal region of C57B/6 mice. As a control, an equal dose of free SQBs in PBS was administrated *via* bolus injection (Fig. 5A and Fig. S6A).

Whole-body fluorescence imaging was performed on days 0, 3 and 7 using IVIS, followed by *ex vivo* analysis of excised tissues on day 10. On day 0, strong Cy5.5 fluorescence signals were detected at all implantation sites, confirming successful delivery (Fig. 5B and Fig. S6B). By day 3, the fluorescence was no longer detectable in the free SQB group, indicating rapid clearance of unencapsulated nanostructures. Notably, while free SQBs were completely cleared within 3 days, prominent and localized fluorescence signals persisted in all hydrogel groups.

Quantitative analysis (Fig. 5C) revealed that the mean fluorescence intensity in hydrogel-treated mice decreased gradually, retaining $79 \pm 6\%$ on day 3 and $41 \pm 10\%$ on day 7 relative to initial levels. This stands in contrast to the free SQB control, which was completely cleared within 3 days, leaving no detectable signal. While all hydrogel formulations demonstrated similar decline trends with no statistically significant
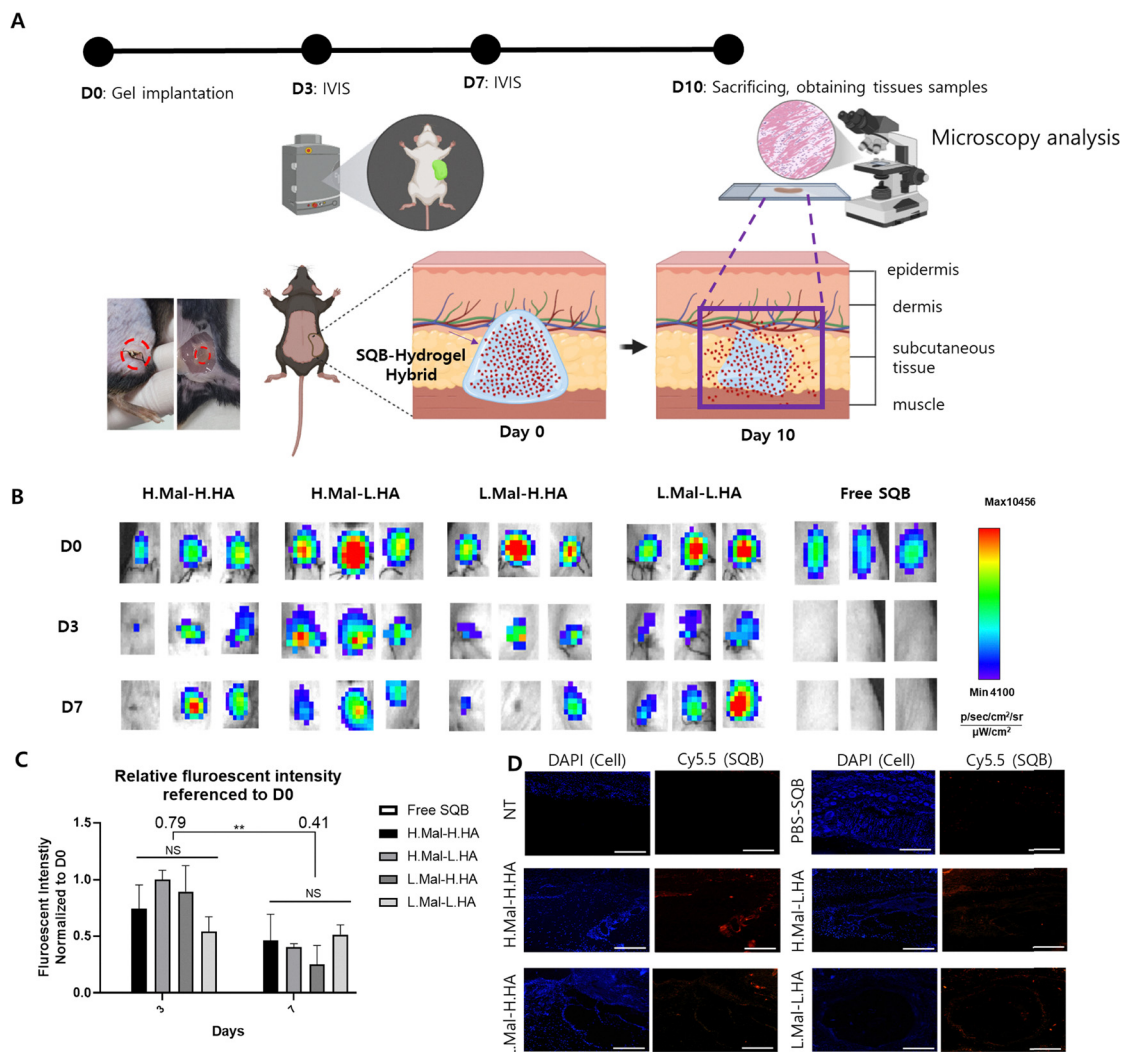
Fig. 5 *In vivo* analysis on sustained release and stability of SQB-hydrogel hybrids. (A) Schematic description of *in vivo* experimental setup. Treatment schedule, IVIS imaging, and histology analysis methods are depicted. (B) IVIS images of mice surgically implanted on subcutaneous layer with fluorescently labeled hydrogels at 0, 3, and 7 days. Pseudo-color images indicate fluorescence intensity from the hydrogel embedded SQBs. (C) Quantification of fluorescence intensity from ROI analysis over time ($n = 3$ per group), showing prolonged retention of SQB−Cy5.5 in hydrogel groups compared to free SQB. The normalized mean fluorescence intensity of hydrogel groups decreased to 0.79 on day 3 and 0.41 on day 7. Statistical analysis was performed using ANOVA with Sidak's *post hoc* test (**$p < 0.01$). (D) Histological imaging of Cy5.5-labeled hydrogels in tissue sections. Representative fluorescence images of tissue sections harvested at day 10 post-implant. Cy5.5-labeled SQB (red) indicate structure-maintained SQBs released to the nearby tissues and remaining inside the hydrogel, while nuclei were stained with DAPI (blue). Scale bars: 500 μm.

differences between them at each time point, the data collectively underscore that the hydrogel matrix offered comparable and robust retention against the rapid physiological clearance that typically limits DNA nanostructures.

To further confirm SQB persistence and local distribution, tissues were excised and sectioned for histological imaging on day 10 (Fig. 5D and Fig. S6C). Consistent with the IVIS results, no detectable Cy5.5 signal remained in the free SQB groups. Conversely, tissues surrounding the hydrogel implantation sites exhibited clearly retained fluorescence, suggesting the gradual release and extended presence of SQBs *in vivo*. The fact that fluorescence was maintained through day 10 highlights the capability of the hydrogel to serve as a long-term depot, effectively maintaining the local concentration of DNA nanostructures far beyond their natural half-life *in vivo*.

Overall, these findings demonstrate that the SQB-hydrogel hybrid serves a dual function: it provides a protective microenvironment that preserves the structural integrity of DNA nanostructures while facilitating their sustained delivery. The prolonged *in vivo* retention, consistent with the *in vitro* sustained release kinetics, confirms the platform's potential to overcome the primary hurdles in DNA nanotechnology—specifically enzymatic instability and rapid clearance—thereby paving the way for long-term, localized therapeutic applications.

4. Conclusions

In this study, we developed a biocompatible hydrogel platform composed of thiolated HA and gelatin, engineered through a synergistic dual-crosslinking mechanism involving maleimide–thiol chemistry and thermal gelation. By modulating the ratios of HA, gelatin, and maleimide, we generated formulations with distinct degradation behaviors, enabling predictable control over SQB release. Crucially, K_{10}-PEG-coated SQBs maintained their structural integrity under enzymatic and serum-rich conditions, and uniformly integrated within the hydrogel variants without aggregation.

Integrated analyses of fluorescence retention, rheological degradation, and SQB release profiles revealed that release kinetics arise from the interplay of restricted diffusion, thermal softening, and enzymatic matrix erosion. This mechanism yields composition-dependent and tunable release profiles rather than relying on a single optimal formulation. Cellular studies using RAW 264.7 macrophages demonstrated that hydrogel-mediated release ensures sustained intracellular SQB availability over several days, contrasting with the rapid uptake and clearance observed with free SQBs. *In vivo* imaging further confirmed the prolonged local retention of SQB–hydrogel hybrids compared to free nanostructures.

Collectively, this work establishes a versatile and protective system that stabilizes DNA nanostructures and enables programmable release through rational material design. A defining feature of this platform is its decoupled architecture: unlike conventional DNA hydrogels where the DNA itself serves as the structural matrix, our system employs a decoupled architecture:

DNA origami SQBs function as discrete nanoparticles, while the HA/gelatin hydrogel independently dictates mechanics, degradation, and the stabilizing ionic environment. This separation of roles facilitates scalable fabrication, preserves the full programmability of DNA nanostructures, and allows matrix properties to be tuned without altering nanostructure design. Such modularity highlights the conceptual distinction of this platform and expands the design space for the hydrogel-assisted delivery of structurally defined DNA materials.

Author contributions

Youngjin Choi and Yeonju Song contributed equally to this work. Youngjin Choi: writing – original draft, investigation, methodology, formal analysis, validation. Yeonju Song: writing – original draft, investigation, formal analysis, validation. Bo Kyung Cho: investigation. Sang Jin Baek: investigation. Jin Myeong Wang: investigation. Su Hyun Seok: investigation. William M. Shih: review & editing. Junsang Doh: writing – review & editing, Supervision. Youngmee Jung: writing – review & editing, conceptualization, supervision. Ju Hee Ryu: writing – review & editing, conceptualization, supervision. All authors discussed the results and commented on the manuscript.

Conflicts of interest

The authors declare no conflict of interest.

Data availability

The data supporting this article have been included as part of the supplementary information (SI). Supplementary information is available. See DOI: https://doi.org/10.1039/d5nh00846h.

Additional data supporting the findings of this study are available from the corresponding author upon reasonable request.

Acknowledgements

References

1 G. Z. Li, C. Y. Chen, Y. Y. Li, B. Wang, J. L. Wen, M. Y. Guo, M. Chen, X. B. Zhang and G. L. Ke, *Nano Lett.*, 2024, **24**, 11335–11348.

2 P. F. Zhan, A. Peil, Q. Jiang, D. F. Wang, S. Mousavi, Q. C. Xiong, Q. Shen, Y. X. Shang, B. Q. Ding, C. X. Lin, Y. G. Ke and N. Liu, *Chem. Rev.*, 2023, **123**, 3976–4050.

3 S. M. Douglas, H. Dietz, T. Liedl, B. Högberg, F. Graf and W. M. Shih, *Nature*, 2009, **459**, 414–418.

4 Y. G. Ke, S. M. Douglas, M. H. Liu, J. Sharma, A. C. Cheng, A. Leung, Y. Liu, W. M. Shih and H. Yan, *J. Am. Chem. Soc.*, 2009, **131**, 15903–15908.

5 Y. C. Zeng, O. J. Young, C. M. Wintersinger, F. M. Anastassacos, J. I. MacDonald, G. Isinelli, M. O. Dellacherie, M. Sobral, H. Bai, A. R. Graveline, A. Vernet, M. Sanchez, K. Mulligan, Y. Choi, T. C. Ferrante, D. B. Keskin, G. G. Fell, D. Neuberg, C. J. Wu, D. J. Mooney, I. C. Kwon, J. H. Ryu and W. M. Shih, *Nat. Nanotechnol.*, 2024, **19**, 1055–1065.

6 B. J. H. M. Rosier, A. J. Markvoort, B. G. Audenis, J. A. L. Roodhuizen, A. den Hamer, L. Brunsveld and T. F. A. de Greef, *Nat. Catal.*, 2020, **3**, 295–306.

7 R. Veneziano, T. J. Moyer, M. B. Stone, E. C. Wamhoff, B. J. Read, S. Mukherjee, T. R. Shepherd, J. Das, W. R. Schief, D. J. Irvine and M. Bathe, *Nat. Nanotechnol.*, 2020, **15**, 716–723.

8 T. Fang, J. Alvelid, J. Spratt, E. Ambrosetti, I. Testa and A. I. Teixeira, *ACS Nano*, 2021, **15**, 3441–3452.

9 J. Yin, S. Y. Wang, J. H. Wang, Y. W. Zhang, C. H. Fan, J. Chao, Y. Gao and L. H. Wang, *Nat. Mater.*, 2024, **23**, 854–862.

10 J. Spratt, J. M. Dias, C. Kolonelou, G. Kiriako, E. Engström, E. Petrova, C. Karampelias, I. Cervenka, N. Papanicolaou, A. Lentini, B. Reinius, O. Andersson, E. Ambrosetti, J. L. Ruas and A. I. Teixeira, *Nat. Nanotechnol.*, 2024, **19**, 237–245.

11 B. Chen, L. Mei, Y. G. Wang, H. Li, C. Q. Feng, M. Mu, R. R. Fan, B. W. Zou and G. Guo, *Small Methods*, 2025, **9**, 2401993.

12 L. Mei, B. Chen, R. R. Fan, M. Wu, C. X. Weng, A. P. Tong, B. W. Zou, H. Yang, C. L. Nie and G. Guo, *Adv. Funct. Mater.*, 2022, **32**, 2112544.

13 L. Li, S. Nie, T. Du, J. Zhao and X. Chen, *MedComm – Biomater. Appl.*, 2023, **2**, e37.

14 S. Li, Q. Jiang, S. Liu, Y. Zhang, Y. Tian, C. Song, J. Wang, Y. Zou, G. J. Anderson, J.-Y. Han, Y. Chang, Y. Liu, C. Zhang, L. Chen, G. Zhou, G. Nie, H. Yan, B. Ding and Y. Zhao, *Nat. Biotechnol.*, 2018, **36**, 258–264.

15 F. Xu, Q. Xia and P. F. Wang, *Front. Chem.*, 2020, **8**, 751.

16 D. W. Jiang, Z. L. Ge, H. J. Im, C. G. England, D. L. Ni, J. J. Hou, L. H. Zhang, C. J. Kutyreff, Y. J. Yan, Y. Liu, S. Y. Cho, J. W. Engle, J. Y. Shi, P. Huang, C. H. Fan, H. Yan and W. B. Cai, *Nat. Biomed. Eng.*, 2018, **2**, 865–877.

17 E. C. Wamhoff, G. A. Knappe, A. A. Burds, R. R. Du, B. W. Neun, S. Difilippantonio, C. Sanders, E. F. Edmondson, J. L. Matta, M. A. Dobrovolskaia and M. Bathe, *ACS Appl. Bio. Mater.*, 2023, **6**, 1960–1969.

18 S. Messaoudi, A. A. Greschner and M. A. Gauthier, *Adv. Therap.*, 2019, **2**, 1900144.

19 B. Han, Y. Song, J. Park and J. Doh, *J. Controlled Release*, 2022, **343**, 379–391.

20 S. Ramakrishnan, H. Ijäs, V. Linko and A. Keller, *Comput. Struct. Biotechnol.*, 2018, **16**, 342–349.

21 Y. X. Liu, R. X. Wang, Q. M. X. Chen, Y. Chang, Q. Chen, K. Fukumoto, B. X. Wang, J. C. Yu, C. F. Luo, J. Y. Ma, X. X. Chen, Y. Murayama, K. Umeda, N. Kodera, Y. Harada, S. Sekine, J. F. Li and H. Tadakuma, *Nano Lett.*, 2024, **24**, 8410–8417.

22 N. Ponnuswamy, M. M. C. Bastings, B. Nathwani, J. H. Ryu, L. Y. T. Chou, M. Vinther, W. A. Li, F. M. Anastassacos, D. J. Mooney and W. M. Shih, *Nat. Commun.*, 2017, **8**, 15654.

23 M. Nasiri, M. Bahadorani, K. Dellinger, S. Aravamudhan, J. L. Vivero-Escoto and R. Zadegan, *Int. J. Biol. Macromol.*, 2024, **260**, 129495.

24 C. Lachance-Brais, M. Rammal, J. Asohan, A. Katolik, X. Luo, D. Saliba, A. Jonderian, M. J. Damha, M. J. Harrington and H. F. Sleiman, *Adv. Sci.*, 2023, **10**, e2205713.

25 L. Tang, S. Wu, Y. Xu, Y. Li, B. Dai, C. Yang, A. Liu, J. Tang and L. Gong, *Adv. Mater. Technol.*, 2022, **7**, 2200066.

26 M.-A. Shahbazi, T. Bauleth-Ramos and H. A. Santos, *Adv. Therap.*, 2018, **1**, 1800042.

27 Y. Lei, M. Rahim, Q. Ng and T. Segura, *J. Controlled. Release*, 2011, **153**, 255–261.

28 D. Yamaguchi, M. Yoshida and S.-I. Nakano, *DNA*, 2022, **2**, 302–313.

29 L. A. Torres-de la Roche, V. Bérard, M. S. de Wilde, R. Devassy, M. Wallwiener and R. L. De Wilde, *J. Clin. Med.*, 2022, **11**, 931.

30 O. J. Young, H. Dembele, A. Rajwar, I. C. Kwon, J. H. Ryu, W. M. Shih and Y. C. Zeng, *Small Methods*, 2025, **9**, 2401376.

31 S. P. Zustiak and J. B. Leach, *Biomacromolecules*, 2010, **11**, 1348–1357.

32 E. Axpe, D. Chan, G. S. Offeddu, Y. Chang, D. Merida, H. L. Hernandez and E. A. Appel, *Macromolecules*, 2019, **52**, 6889–6897.

33 S. Ramakrishnan, G. Krainer, G. Grundmeier, M. Schlierf and A. Keller, *Small*, 2017, **13**, 1702100.

34 V. Linko and A. Keller, *Small*, 2023, **19**, 2301935.